The International Journal of Advanced Manufacturing Technology (2025) 140:4845–4858
https://doi.org/10.1007/s00170-025-16581-w

ORIGINAL ARTICLE

Effect of external magnetic field on arc characteristics and weld bead formation in metal-cored arc welding

Van Hanh Bui[1] · Quang Ngoc Trinh[1,2] · Dang Khoi Le[2] · Shinichi Tashiro[2] · Le Duy Han[1] · Huy Le Phan[1] · Anthony B. Murphy[3] · Kenta Yamanaka[4] · Manabu Tanaka[2] · Lei Xiao[5]

Received: 8 April 2025 / Accepted: 12 September 2025 / Published online: 27 September 2025

Abstract

This study aimed to clarify the influence of a longitudinal external magnetic field (EMF) on arc characteristics, metal transfer behavior, and weld bead formation in metal-cored arc welding (MCAW) process. The work focused on comparing two distinct conditions: without EMF (0 mT) and with EMF applied at a magnetic flux density (MFD) of 6 mT, evaluated by high-speed video observations and numerical simulation models for a welding current of 320 A. Experimental results indicated negligible changes in droplet transfer frequency between the two conditions, but significant differences were observed in arc behavior and weld pool characteristics. The application of EMF intensified arc brightness and increased weld penetration depth from 3.7 mm (no EMF) to 4.2 mm (EMF 6 mT). Simulation results revealed that EMF induced rotational plasma flow and reduced pressure at the arc column center, which resulted in an increased plasma velocity directed toward the weld pool surface. Consequently, a depression was observed at the weld pool surface to enhance the weld bead penetration. The findings highlight the potential of EMF as a valuable tool to optimize MCAW processes, particularly when precise penetration control and improvement of weld quality are required.

Keywords External magnetic field · Metal-cored arc welding · Weld pool observation · Arc plasma simulation · Arc pressure

1 Introduction

Gas metal arc welding (GMAW) is widely employed in various industrial applications owing to its high productivity, ease of automation, and consistent weld quality. In the GMAW process, metal droplets are formed at the tip of a continuously fed solid electrode and transferred into the weld pool [1]. The metal transfer process significantly influences the weld bead geometry and mechanical properties of welded joints [2]. Thus, effective control over metal transfer behavior is crucial for ensuring high-quality welds [3].

Metal-cored arc welding (MCAW), an advanced variant of GMAW, uses a tubular wire filled mainly with metallic powders. MCAW effectively combines several advantages of solid-wire GMAW and flux-cored arc welding (FCAW) with rutile flux powder, including high deposition rates, reduced spatter generation, and minimal slag formation [4–6]. In particular, MCAW maintains stable arc performance at high welding currents around 300 A [7]. These characteristics make MCAW particularly suitable for industries such as shipbuilding, structural steel fabrication, and

✉ Quang Ngoc Trinh
ngoc.trinhquang@hust.edu.vn

✉ Shinichi Tashiro
tashiro.shinichi.jwri@osaka-u.ac.jp

✉ Lei Xiao
xiaolei@lzjtu.edu.cn

[1] School of Mechanical Engineering, Hanoi University of Science and Technology, Hanoi 100-000, Vietnam

[2] Joining and Welding Research Institute, The University of Osaka, Osaka 567-0047, Japan

[3] CSIRO Manufacturing, Lindfield, NSW 2070, Australia

[4] Institute for Materials Research, Tohoku University, 2-1-1 Katahira, Aoba-Ku, Sendai 980-8577, Japan

[5] School of Materials Science and Engineering, Lanzhou Jiaotong University, Lanzhou 730070, China

heavy machinery manufacturing, where productivity and weld quality are paramount [8, 9].

Despite these advantages, the arc phenomena in MCAW are inherently more complex compared to solid-wire GMAW due to the tubular structure of the wire and the presence of internal metallic powders. Recent studies have begun to elucidate aspects of this complexity. For instance, Trinh et al. revealed that the presence of alkaline elements, such as sodium, within the core of MCAW wires has been shown to alter the plasma electrical conductivity and current path [10], thereby significantly affecting the metal transfer frequency and stability. That finding strengthened the findings of Valensi et al. that the alkaline elements supported spray transfer even when a shielding gas with high CO_2 concentration was applied [11]. Furthermore, the effect of such elements was reported to be more significant than wire structure at a high welding current of 320 A, as reported by Bui et al. [7]. Regarding shielding gas influence, the metal-cored wire was observed to limit the instability of the metal transfer under pure argon shielding gas of conventional solid wire [12]. On the other hand, when CO_2 are introduced in the shielding gas, the metal transfer frequency peaked at approximately 15% CO_2 content due to the balance between electromagnetic force and arc pressure in MCAW processes [13]. In rutile flux-cored welding, this optimal CO_2 concentration shifted toward lower values as welding current increased [14]. These studies have provided initial insights into the intricate interplay among wire composition, shielding gas, and arc behavior. In addition, the MCAW process has recently attracted increasing attention, driven by advancements in wire-based additive manufacturing technologies. This growing interest underscores the need for further detailed investigations into MCAW phenomena [15–17].

The quality and mechanical performance of welded joints are strongly influenced by weld bead geometry, which in turn significantly depends on metal transfer behaviors and the interactions between droplets and the weld pool [18]. An unstable metal transfer mode often leads to defects such as gas porosity, lack of fusion, incomplete penetration, and excessive spatter, thereby deteriorating weld quality [19–21]. Therefore, understanding and controlling the metal transfer process are vital for achieving high-quality welds. In addition to conventional mechanical performance evaluation, recent studies have emphasized the importance of assessing corrosion resistance of welded joints, particularly for high-strength aluminum alloys in aerospace and marine applications. For instance, exfoliation corrosion has been shown to significantly deteriorate the performance of hybrid joints produced by friction stir welding (FSW), especially in dissimilar aluminum alloy combinations [22, 23]. These findings indicate that, beyond strength and defect control, corrosion behavior is also a critical factor influencing the long-term reliability of welded joints. Insights from these studies provide a broader context for understanding the mechanisms by which welding conditions affect both internal defect generation and long-term service performance.

Recently, several external-assistance techniques have been proposed to enhance metal transfer control and weld quality. Techniques such as laser-assisted welding [24], ultrasonic-assisted welding [25], and high-frequency pulsed welding have been demonstrated to improve arc stability and reduce spatter generation [26]. Among these methods, applying an external magnetic field (EMF) emerges as a promising approach [27]. Luo et al. reported that electromagnetic stirring (EMS) induced by an external magnetic field significantly improved droplet transfer characteristics, resulting in better weld formation and reduced spatter generation in CO_2 welding [28]. Similar findings were observed by Jiang et al., who showed that applying a longitudinal magnetic field effectively reduced droplet size and improved uniformity in short-circuit transfer frequency, enhancing welding stability [29]. Additionally, Wu et al. revealed that an external magnetic field notably suppressed weld pool instabilities, particularly humping defects, by controlling backward molten metal flow dynamics in high-speed GMAW [30]. Furthermore, Guan et al. indicated that adjusting the frequency of an external magnetic field directly influenced the welding arc shape, microstructure, and mechanical properties of weld beads [31]. Le et al. demonstrated that introducing an external longitudinal magnetic field into conventional CO_2 welding significantly stabilized droplet transfer, reduced droplet size, and mitigated spatter formation, thus enhancing weld quality and joint performance [32]. These results highlight the considerable potential of EMF-assisted welding technology; however, to date, studies applying EMF specifically in MCAW or FCAW processes remain very limited in the literature.

In response to this research gap, the present study investigates the influence of an applied longitudinal EMF on metal transfer behavior, arc characteristics, and weld bead formation in MCAW at a welding current of 320 A. Experiments were conducted under two distinct conditions: without EMF (0 mT) and EMF applied at a magnetic flux density (MFD) of 6 mT. High-speed imaging techniques, including shadowgraph imaging and laser-assistance illumination, were employed to observe the droplet transfer behaviors and the dynamics of the weld pool surface. Additionally, a numerical simulation was performed to elucidate the physical mechanisms underlying the influence of EMF on the arc, particularly focusing on arc plasma temperature and velocity distribution. The combined experimental and simulation approaches aim to provide a comprehensive understanding of how EMF influences MCAW performance, contributing valuable insights for advancing high-current MCAW applications.

2 Experiment procedure and simulation model

2.1 Welding conditions

In this study, a single weld bead was deposited on a mild steel plate (SS400 – JIS G 3101) with dimensions of 300 × 50 × 9 mm. A commercial metal-cored wire electrode, corresponding to AWS A5.20 E71T-1C, with a diameter of 1.2 mm diameter was investigated. The detailed composition of the base metal and filler material is provided in Table 1.

Figure 1 illustrates the principle of experimental setup employed in this study for observing metal transfer behavior and weld pool dynamics under the influence of EMF. To generate a longitudinal EMF, a cylindrical excitation coil with 100 turns was positioned concentrically around the welding torch nozzle. MFD was controlled precisely at two levels, 0 mT (no EMF) and 6 mT, by adjusting the supplied current from a direct current (DC) power source.

The welding experiments were performed using a DP-350 (OTC Daihen) welding power source operating in direct current electrode positive (DCEP) mode, integrated with a standard wire-feeding system. A metal-cored wire was used with a constant welding current of 320 A, and the welding voltage was fixed at approximately 33.5 V. Pure argon was used as shielding gas at a constant flow rate of 20 L/min. The contact-tip-to-work distance (CTWD) was maintained

Table 1 Composition of base metal and filler material

	Elements								
	C	Si	Mn	P	S	Al	SiO_2	TiO_2	Fe
Base metal	0.26	0.40	-	0.04	0.05	-	-	-	Bal
Filler material	0.04	0.90	2.00	-	-	0.26	0.23	0.33	Bal

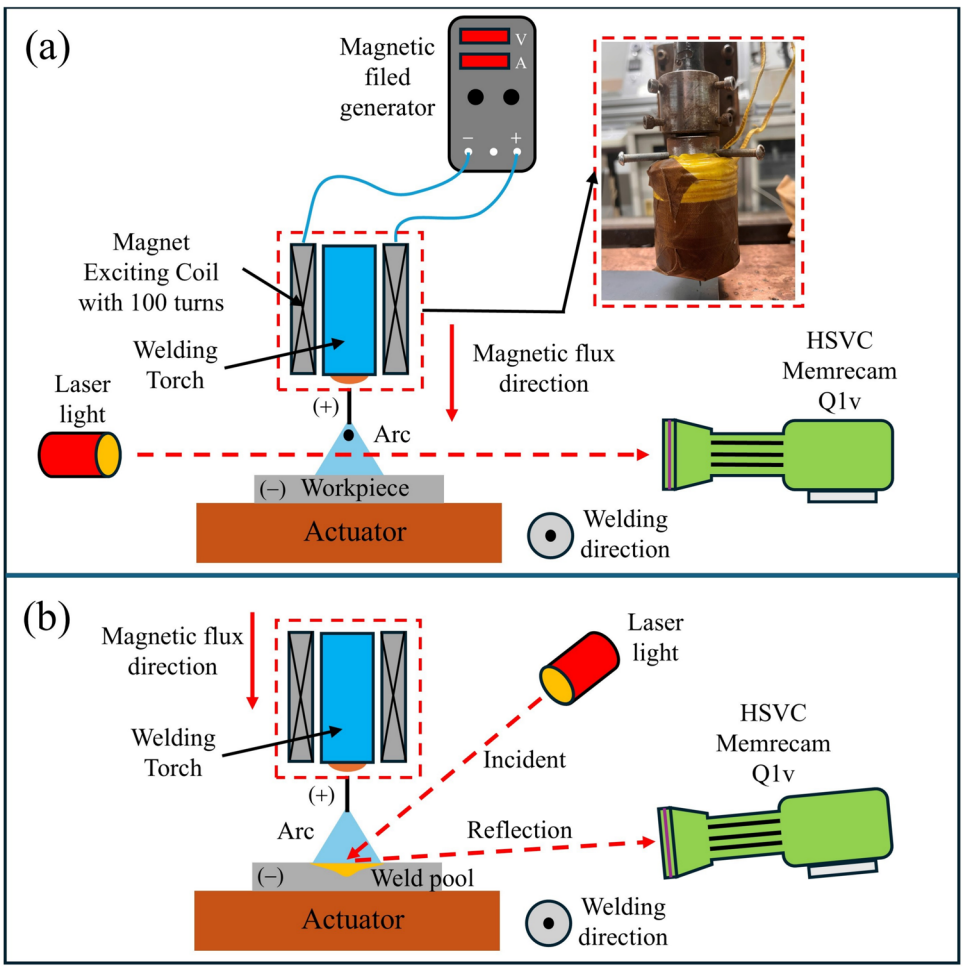

Fig. 1 Schematic experimental setup for **a** metal transfer behavior observation and **b** weld pool observation

consistently at 20 mm, and the wire extension was kept at 10 mm above the workpiece surface prior to welding. The coil was coaxial with the contact tip of the welding torch. The longitudinal MFD at the wire end, 10 mm from both the contact tip and the lower end of the coil, was measured using a teslameter. When the excitation current reached 3 A, the MFD at this location reached 6 mT. The cylindrical coil employed in this experiment was a solenoid coil with an iron core, and its design is illustrated in Fig. 1. During welding, the workpiece was translated at a constant speed of 5 mm/s using a motorized actuator.

2.2 Observation conditions

In Fig. 1a, the observation setup for the arc characteristics and metal transfer with the shadowgraph method is depicted, in which the apparatus arrangement is similar to a previous work [13]. A schematic of the experimental setup for weld pool surface observation is depicted in Fig. 1b. Due to the intensive radiation emitted from the welding arc, direct visualization of the weld pool was challenging. Therefore, a laser-assisted high-speed camera system was employed to improve image clarity and visibility of weld pool dynamics. In this setting, the laser was positioned on the same side as the camera, directing intense illumination toward the weld pool surface. The intensity of the laser illumination at the 640-nm wavelength significantly exceeded the arc radiation intensity at the same wavelength, enabling clear differentiation of the weld pool from the surrounding arc plasma. The reflected laser illumination from the weld pool surface was captured using a high-speed video camera equipped with a bandpass filter centered at 640 nm. The distance from the camera to the observation point was approximately 600 mm. Additionally, to further reduce residual arc radiation, neutral-density filters (ND8) were installed in front of the camera lens. The observation parameters are shown in detail in Table 2.

Table 2 Observation parameters

Parameters	Value
Camera	Nac, Memrecam Q1V
Lens	AF Micro-NIKKOR
Focal length	105 mm
Focal ratio	1/2.8
Frame rate	4000 fps
Exposure time	26 μs
Aperture	f/5.6
Neutral filter	Five ND8 for metal transfer observation. Two ND8 and laser filter for weld pool observation
Laser wavelength	640 nm

2.3 Simulation model

A Computational fluid dynamics (CFD) simulation was conducted to provide deeper insights into underlying physical mechanisms, particularly focusing on the arc plasma characteristics such as temperature distribution, plasma velocity, arc pressure, and metal vapor concentration. The numerical simulation aimed to clarify physical phenomena difficult to measure experimentally, enhancing understanding of observed experimental results.

The computational domain was constructed as a rectangular volume of 40 mm × 40 mm × 20 mm along the *X*, *Y*, and *Z* axes, respectively. The CTWD was 20 mm, and the arc length was maintained at 5 mm. The welding current was fixed at 320 A. EMF formed by the cylindrical excitation coil was assumed to have a constant magnitude in the Z direction. Here, two EMF conditions were considered: no magnetic field (0 mT) and MFD of 6 mT.

We have developed a simplified simulation model assuming a steady state, ignoring the deformation and detachment of the droplet. The model specifically considered metal vapor effects on the plasma temperature field, plasma velocity field, and pressure field to elucidate the influence of EMF. A set of governing equations, including the conservation equations of mass, mass of metal vapor, momentum, energy, current, and the supplementary equations, was solved as follows:

Mass conservation:

$$\nabla \cdot \left(\rho \vec{u}\right) = 0 \tag{1}$$

Mass conservation of metal vapor:

$$\nabla \cdot \left(\rho Y \vec{u}\right) = \nabla \cdot (\rho D \nabla Y) + M_{mv} \tag{2}$$

Momentum conservation:

$$\nabla \cdot \left(\rho \vec{u}\vec{u}\right) = -\nabla p + \nabla \cdot \vec{\vec{\tau}} + \rho \vec{g} + \vec{j} \times \vec{B} \tag{3}$$

Energy conservation:

$$\nabla \cdot \left(\rho h \vec{u}\right) = \nabla \cdot (k \nabla T) + \vec{j} \cdot \vec{E} - Q_r \tag{4}$$

Current conservation:

$$\nabla \cdot \sigma \nabla \Phi = 0 \tag{5}$$

Ohm's law:

$$\vec{j} = -\sigma \nabla \Phi = \sigma \vec{E} \tag{6}$$

Vector potential:

$$\nabla^2 \vec{A} = -\mu_0 \vec{j} \tag{7}$$

Magnetic field:

$$\vec{B} = \nabla \times \vec{A} \tag{8}$$

where ρ is the mass density, $\vec{u}$ is the velocity, Y is the mass fraction of metal vapor, D is the diffusion coefficient of metal vapor, M_{mv} is the source term for evaporation of metal, p is the pressure, $\vec{\tau}$ is the viscous stress tensor, $\vec{g}$ is the gravity, $\vec{j}$ is the current density, $\vec{B}$ is the magnetic field,$\vec{F_s}h$ is the enthalpy, k is the thermal conductivity, T is the temperature, $\vec{E}$ is the electric field, Q_r is the source term for arc radiation loss, s is the electrical conductivity, Φ is the electric potential, μ_0 is the magnetic permeability of free space, and $\vec{A}$ is the vector potential.

The above equations and the boundary conditions were similar to the previous study [33]. The temperature field in the wire and droplet was fixed, especially giving a constant temperature of 2600 K in the droplet. The thermodynamic and transport properties of a mixture of argon and iron vapor were calculated as functions of temperature and iron vapor concentration [34, 35]. The model effectively captured the essential arc phenomena and provided detailed information on the plasma arc characteristics under different EMF conditions, which enabled a deeper understanding of the influence of EMF on MCAW processes. The temperature distributions in this study are depicted for half of the entire simulation domain with $X > 20$ mm.

3 Result and discussion

3.1 Experimental result

Figure 2 shows time-sequential shadowgraph images illustrating the arc characteristics and metal transfer behavior observed under two EMF conditions. Both sequences represent one complete metal transfer cycle lasting approximately 4 ms. In both cases, a droplet detached at 0 ms, and a subsequent droplet gradually grew at the wire tip before detaching again at around 4 ms. Measurements from ten separate durations in the recorded movies confirmed that the metal transfer frequencies were similar for both conditions, being 250.3 ± 18.5 Hz and 260.3 ± 7.9 Hz for MFDs of 0 and 6 mT, respectively, which indicated that EMF has negligible influence on the metal transfer frequency.

However, significant differences in arc behavior were observed when EMF was applied. With MFD of 6 mT as shown in Fig. 2b, the arc column appeared more constricted and brighter at the arc center, indicating increased plasma

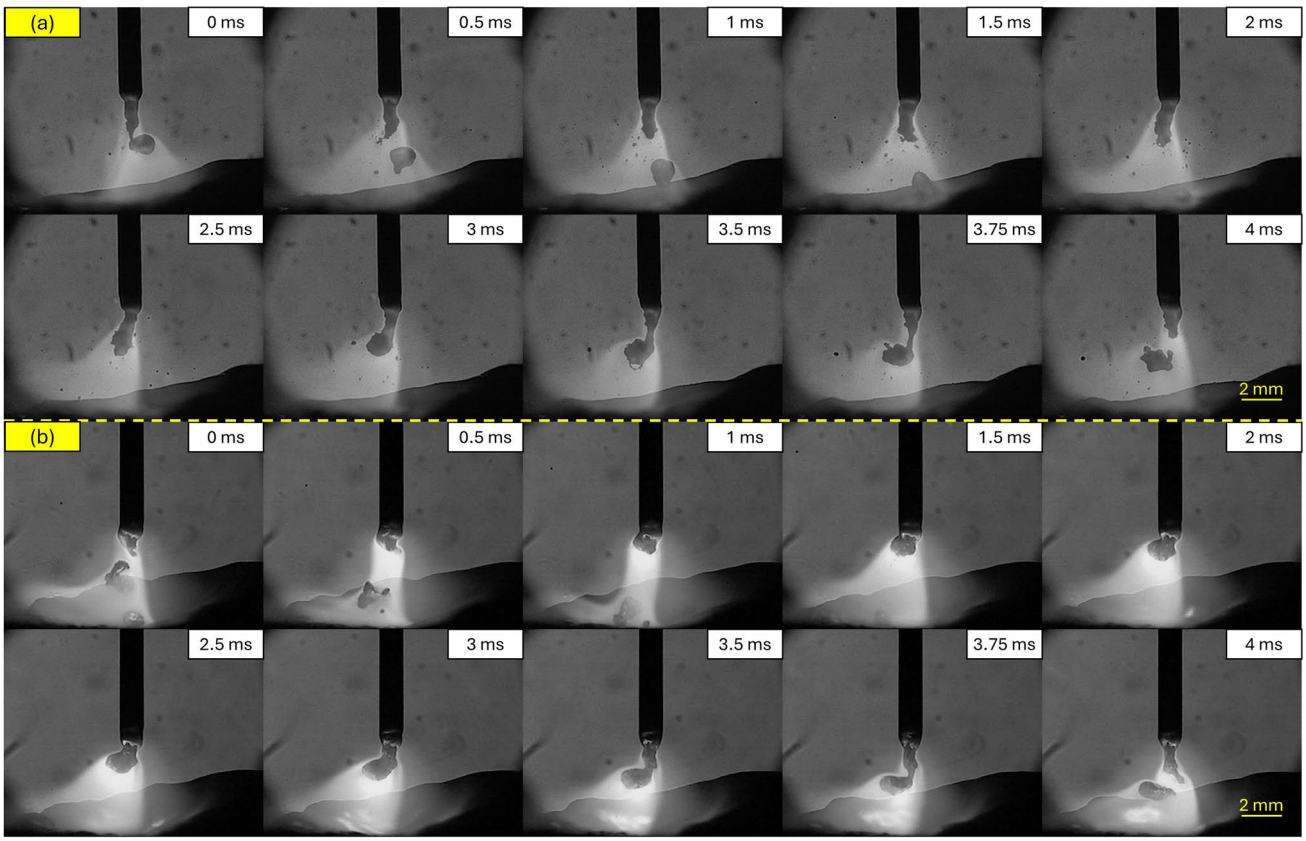

Fig. 2 Time-sequential shadowgraph images of arc characteristics and metal transfer behavior of **a** no EMF and **b** MFD of 6 mT

energy density. This suggests that while EMF does not notably alter the metal transfer frequency, it substantially affects the arc constriction and plasma energy density, potentially influencing weld pool dynamics and penetration depth.

Figure 3 presents time-sequential images of arc and weld pool behavior observed during one complete metal transfer cycle using the laser-assisted illumination under the two EMF conditions. Each cycle duration was approximately 4.25 ms, closely corresponding to the metal transfer cycle depicted in Fig. 2. In Fig. 3a, without EMF, the weld pool surface remained relatively stable and flat throughout the transfer cycle. However, when EMF of 6 mT was applied, a noticeable depression formed at the weld pool surface, suggesting increased arc pressure acting on the weld pool, as observed in Fig. 3b.

To clarify this behavior, typical images captured at the droplet detachment moment and 0.5 ms afterward are presented in Fig. 4. In Fig. 4a, the weld pool surface remains relatively flat. The droplet detached from the wire tip and smoothly entered the weld pool surface with minimal disturbance, and no evident deformation or depression was observed on the weld pool surface. Conversely, applying MFD of 6 mT resulted in a distinct crater-like depression formed on the weld pool surface due to enhanced arc pressure, as observed in Fig. 4b. At the exact moment of droplet detachment (t2 ms), the bottom part of the droplet was partially obscured by the edge of this depression, clearly illustrating the significant impact of the applied magnetic field on weld pool dynamics. This depression persisted and remained clearly visible also at 0.5 ms later. These observations confirmed that while EMF does not significantly alter metal transfer frequency, it notably increased the arc pressure on the weld pool surface, influencing the weld pool behavior and potentially enhancing the weld penetration.

Figure 5 presents a quantitative comparison of the arc brightness intensity observed over a period of 20 ms between the two EMF conditions. The brightness intensity was measured and averaged within a defined rectangular region of 1000 pixels at the middle height of the arc plasma, which was marked by yellow rectangles on the demonstrated images. Five droplet detachments occurred within the observed time interval for each condition.

The brightness intensity consistently decreased just prior to droplet detachment and sharply increased immediately afterward due to the re-establishment of the arc attachment between the wire tip and the weld pool. This behavior corresponds precisely to the visual observations from sequential images.

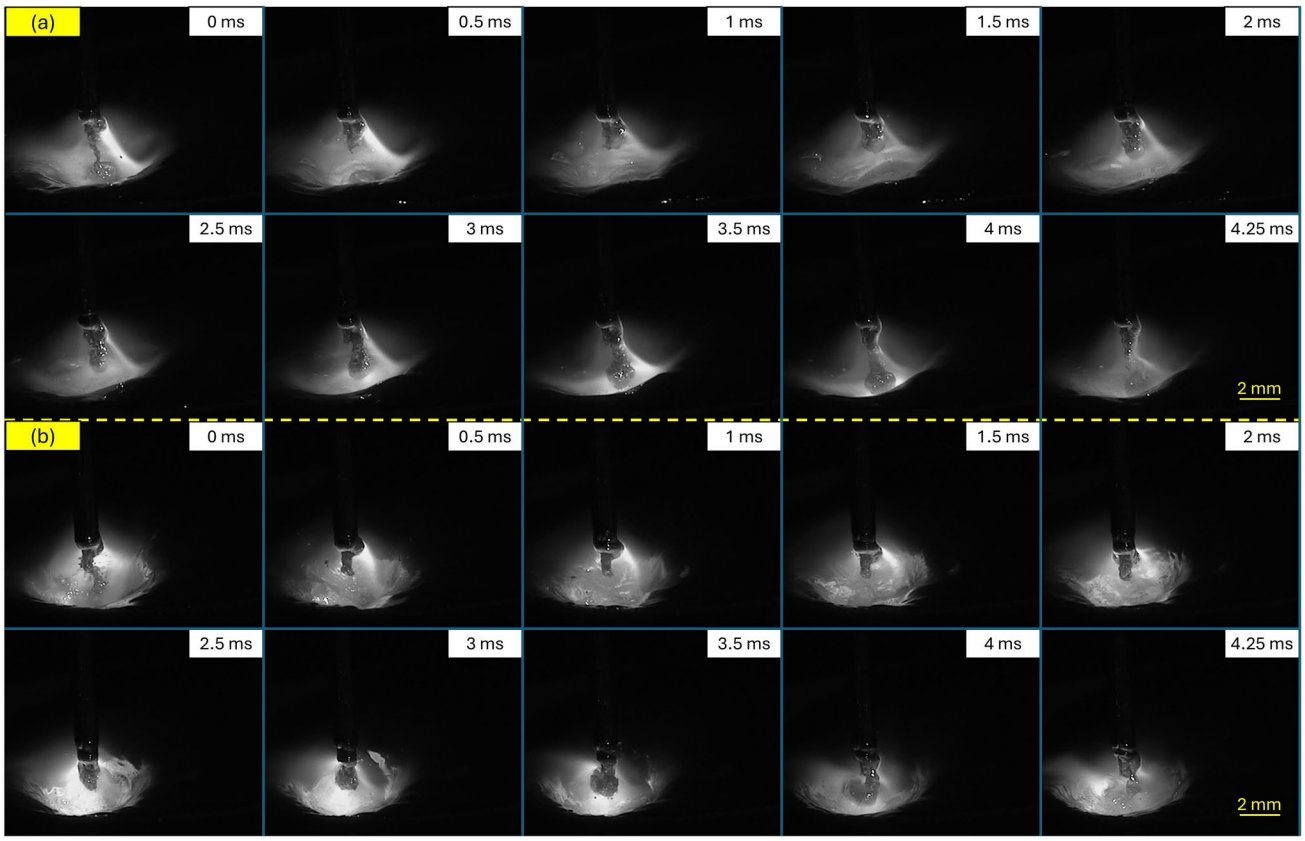

Fig. 3 Time-sequential images of the arc characteristics and weld pool behavior under **a** no EMF and **b** MFD of 6 mT

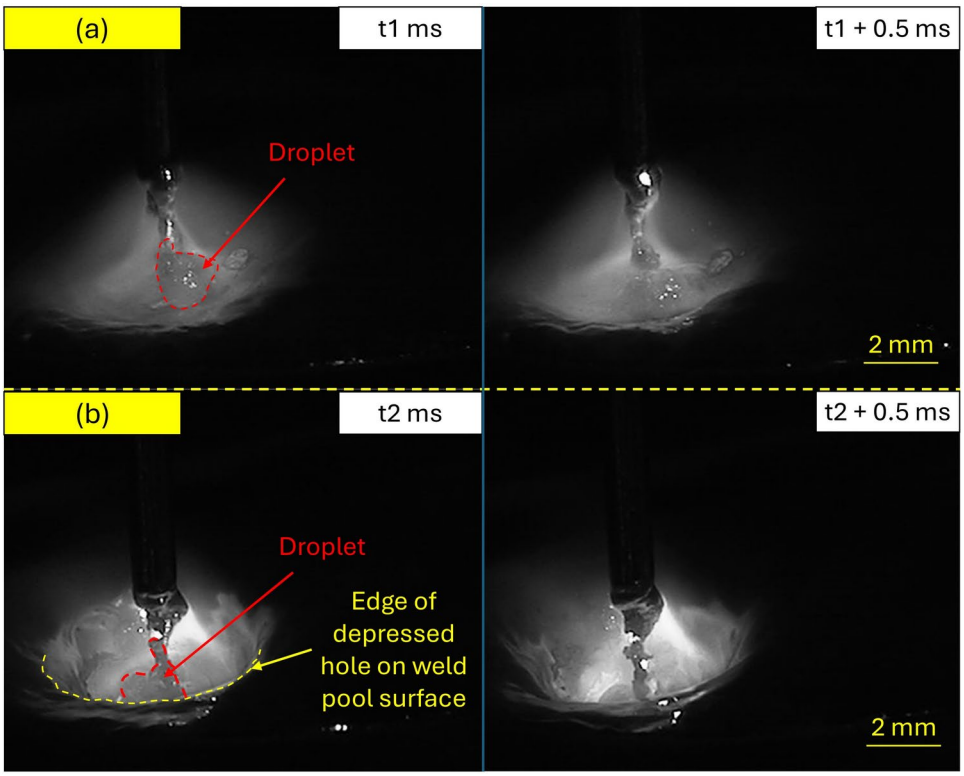

Fig. 4 Typical images for comparison of weld pool behavior between **a** no EMF and **b** MFD of 6 mT

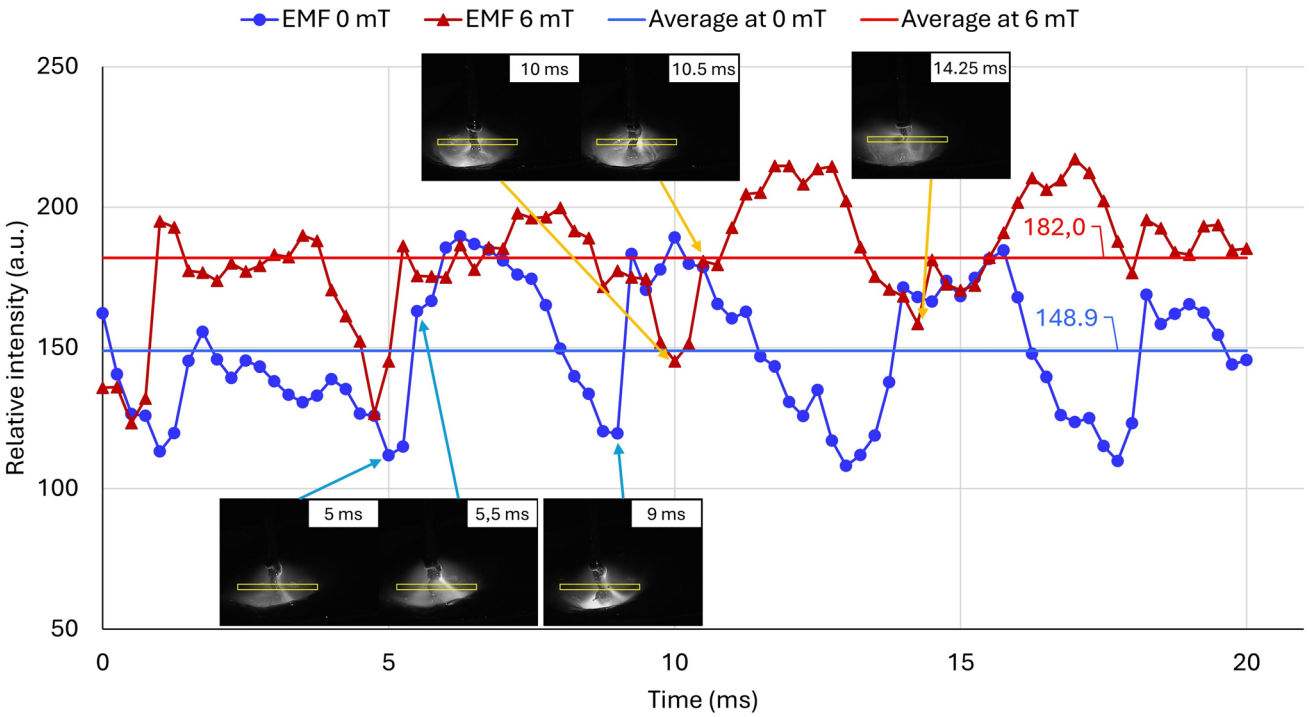

Fig. 5 Comparison of the arc brightness intensity on the image between no EMF and MFD of 6 mT

The average of relative brightness intensity of all time frames in the period was calculated, which significantly increased under the EMF condition, from 148.9 (a.u) to 182.0 (a.u) when the MFD increased from 0 to 6 mT. Because the main constitution of the wire is iron and its oxides, the center of the arc plasma was dominated by the

iron vapor [36]. Thus, the increase in brightness intensity was thought to be caused by a strengthening of metal vapor radiation.

Figure 6 shows representative cross-sectional images of weld beads obtained under the conditions of with and without EMF. The top-surface width and bead height showed negligible differences between the two conditions. Specifically, weld bead widths were 15.3 mm and 15.1 mm for MFD conditions of 0 mT and 6 mT, respectively, while bead heights were identically 3.0 mm in both cases. However, notable differences were observed in weld penetration profiles. The penetration depth increased markedly from 3.7 mm without EMF to 4.2 mm when EMF was applied. Additionally, the width of the fusion boundary region (transition zone from the weld centerline toward the weld edge) expanded from 6.7 to 7.4 mm at MFD of 6 mT. These results clearly indicated that the applied EMF significantly enhanced the weld penetration, confirming the substantial effect of EMF on weld pool dynamics.

3.2 Simulation results

To clarify the influencing mechanism of EMF on the arc and weld pool behavior, a simple simulation was carried out. Figure 7 shows the arc temperature distribution represented by iso-surfaces obtained from numerical simulations under the two EMF conditions.

In both cases, the central region of the arc column exhibited a lower temperature compared to the surrounding area. This phenomenon has been widely reported and is primarily attributed to the presence of iron vapor beneath the droplet [37]. Comparing the two conditions, the size of the lower-temperature region in the arc column center was reduced when applying MFD of 6 mT, as seen in Fig. 7b. This indicates that EMF effectively concentrates the arc column, reducing the volume of the central low-temperature region.

Figure 8 presents the arc temperature distributions on the vertical plane through the wire axis. Similar to observations in Fig. 7, both EMF conditions exhibited a region of lower temperature at the arc column center, which was attributed to the presence of metal vapor beneath the droplet. However, the central low-temperature region is slightly narrower under the EMF condition, also as seen in Figs. 7b and 8b. This more clearly confirms that the applied EMF effectively constricts the arc column, reducing the low-temperature region and intensifying plasma energy concentration.

Figure 9 depicts the iron vapor concentration on the vertical plane through the wire axis under conditions without EMF and with an applied MFD of 6 mT. As clearly depicted in Fig. 9b, applying the EMF notably increased the concentration of metal vapor near the wire tip compared to the without EMF condition shown in Fig. 9a. The simulation in this study focused primarily on arc behavior, incorporating the effect of metal vapor without directly considering the metal transfer process. The elevated concentration of iron vapor seen under EMF conditions significantly reduced the arc center temperature, due to enhanced radiation heat losses from the higher-density vapor region [37].

Figure 10 presents the vertical component of plasma flow velocity on the vertical plane through the wire axis of no EMF and MFD of 6 mT. As clearly shown in Fig. 10b, applying EMF significantly enhanced plasma velocity, particularly at the arc column center. The higher plasma velocity in the arc center under EMF conditions is thought to cause the depletion of weld pool surface as experimentally observed in Fig. 4.

Figure 11 further clarifies the physical mechanism behind these phenomena by showing the distributions of horizontal

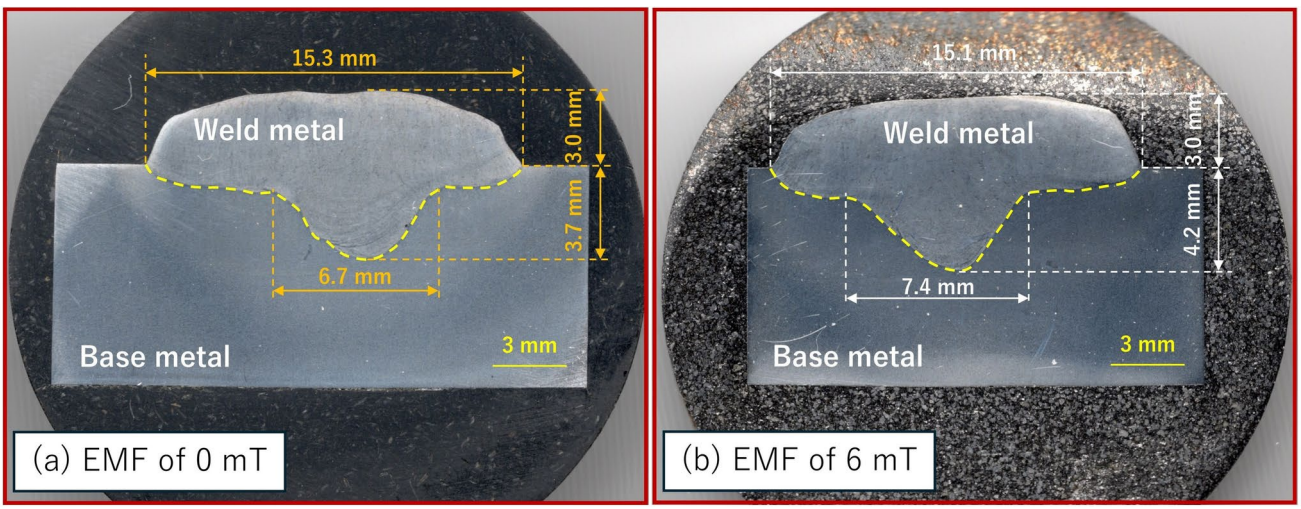

Fig. 6 Photos of the weld bead cross-sections

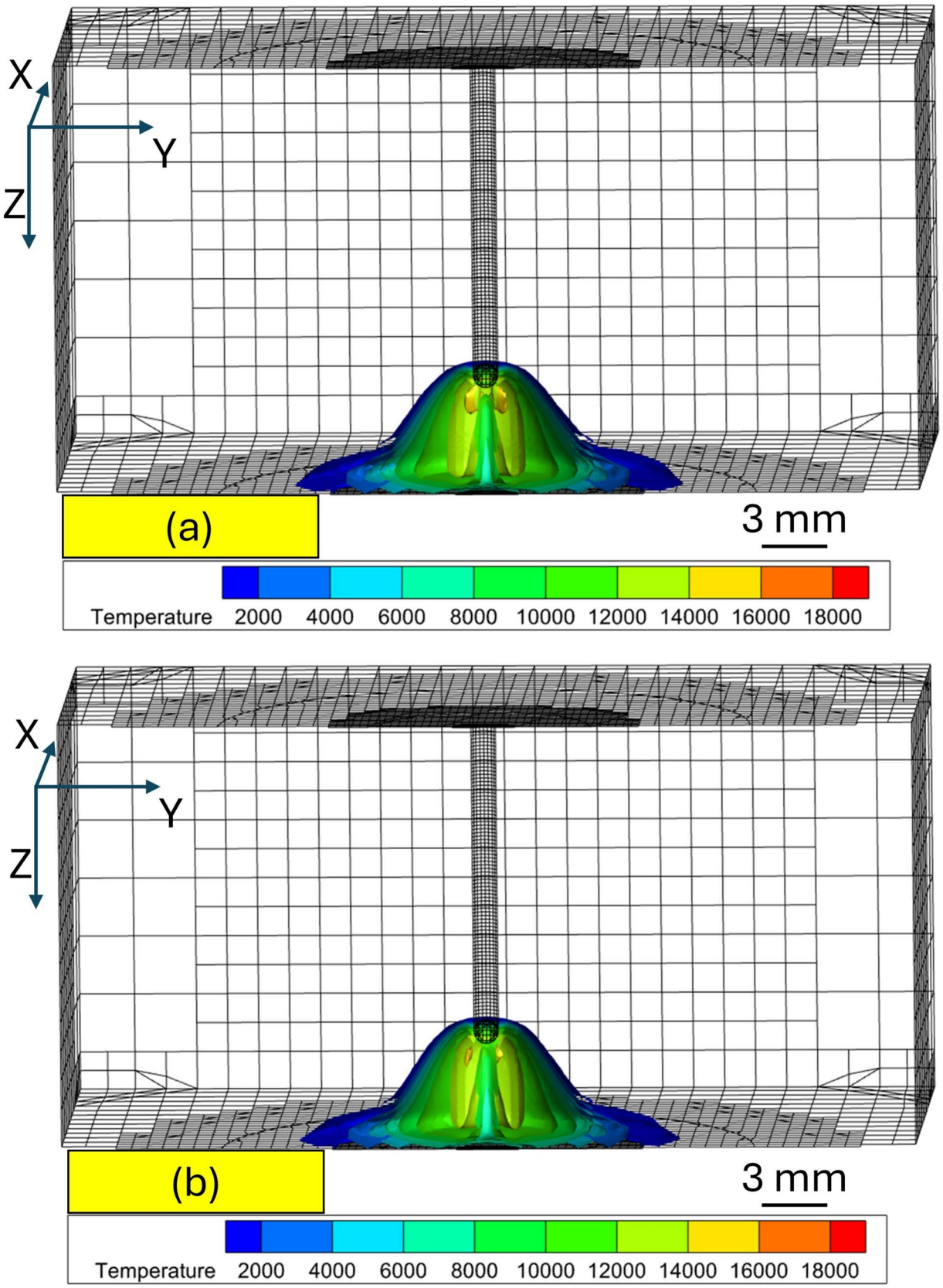

Fig. 7 Arc temperature distribution of **a** no EMF and **b** MFD of 6 mT

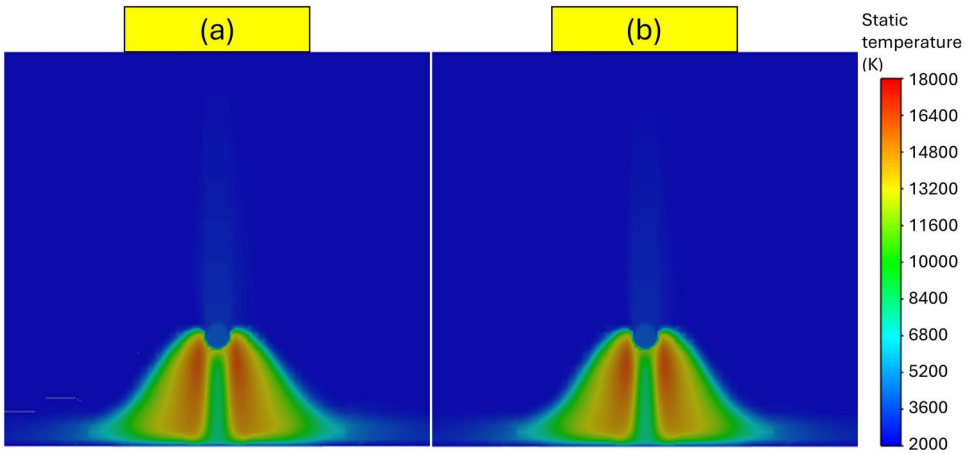

Fig. 8 Arc temperature distribution of **a** no EMF and **b** MFD of 6 mT on the vertical plane through the wire axis

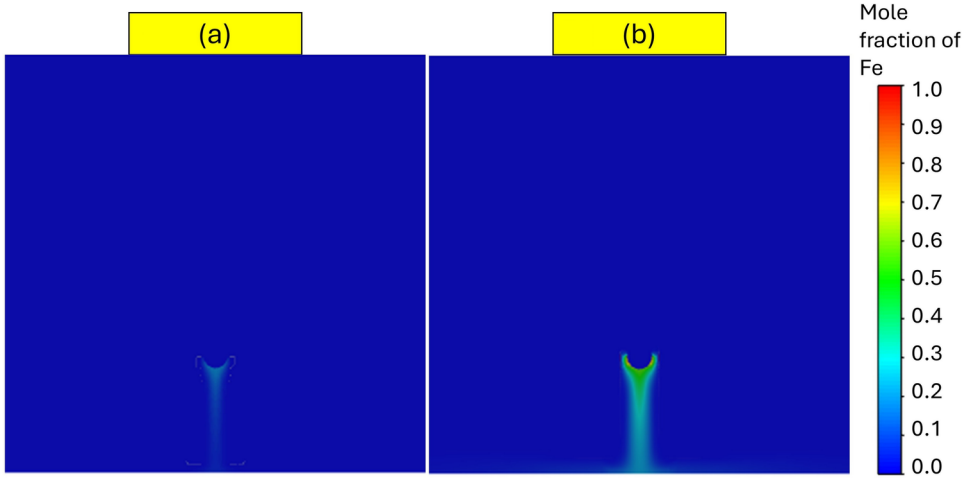

Fig. 9 Iron vapor concentration on the vertical plane through the wire axis of **a** no EMF and **b** MFD of 6 mT

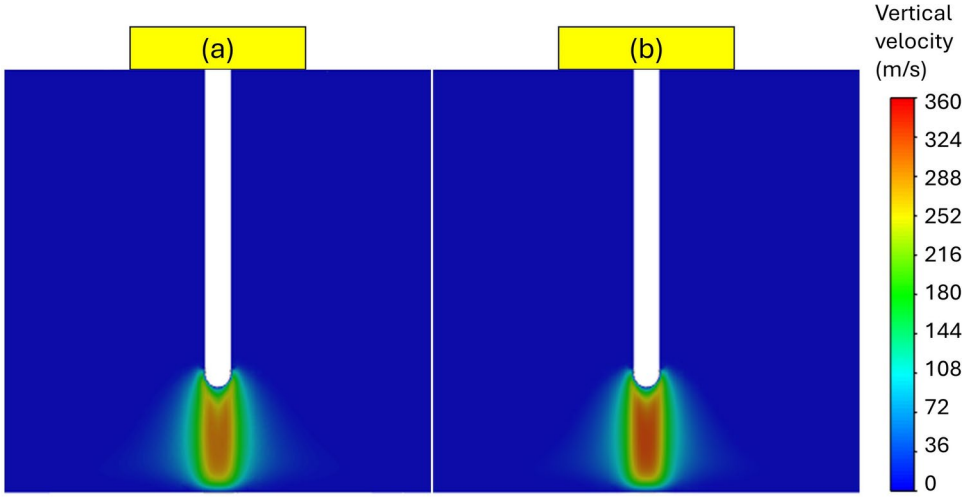

Fig. 10 Vertical component of plasma flow velocity on the vertical plane through the wire axis of **a** no EMF and **b** MFD of 6 mT

component of plasma flow velocity and static pressure at the middle height ($Z = 17.5$ mm) of the arc column under the two EMF conditions. In Fig. 11a, the plasma flowed centripetally to the arc center due to the interaction between the current and self-induced magnetic field around the wire tip. At the center of the arc, the pressure is high. On the other hand, the plasma flowed rotationally around the arc center, as presented in Fig. 11b. When a longitudinal LMF

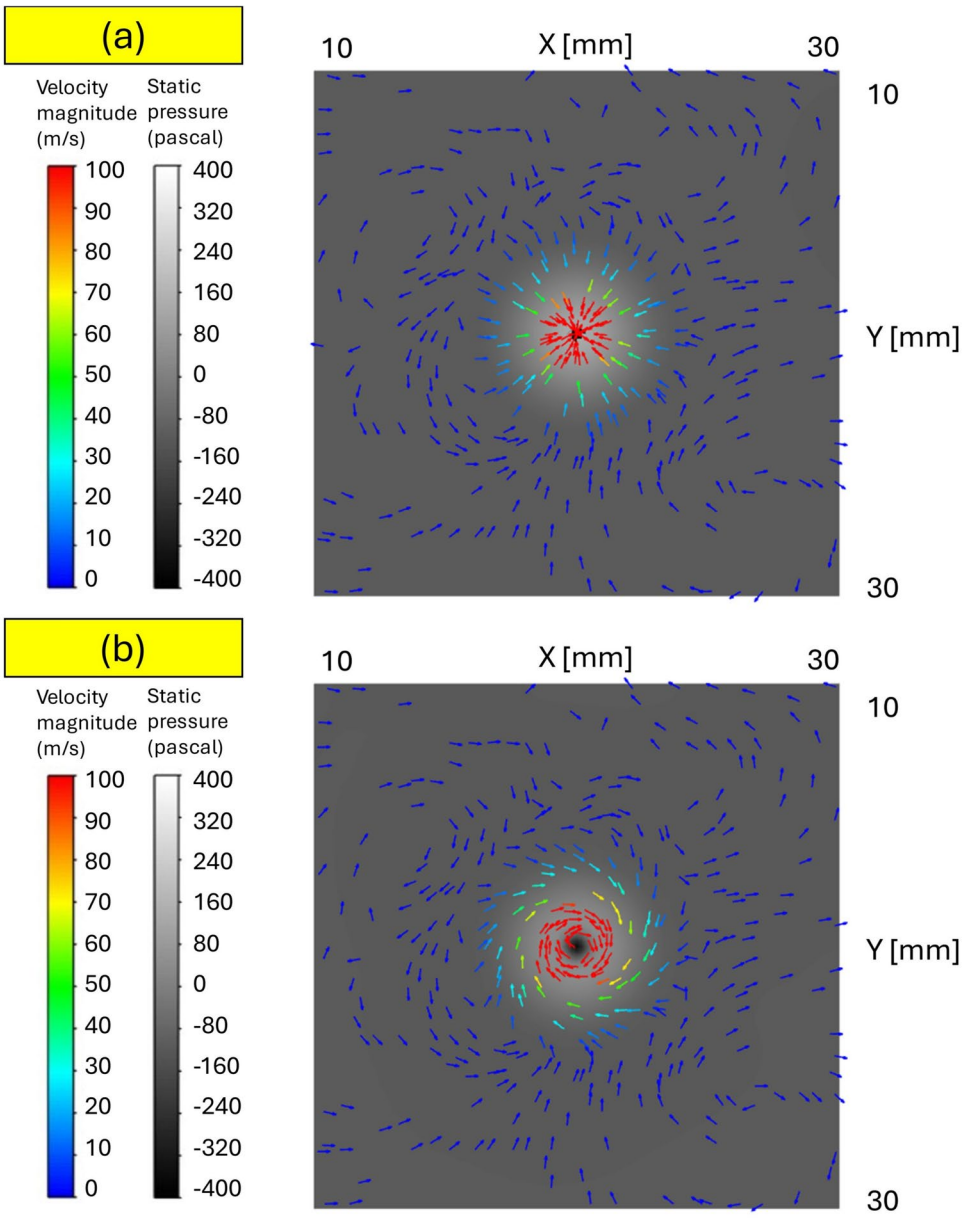

Fig. 11 Distributions of horizontal component of plasma flow velocity and static pressure of **a** no EMF and **b** MFD of 6 mT at middle height of the arc column ($Z = 17.5$ mm)

is applied, the interaction between the radial component of current and LMF produces a Lorentz force in the horizontally rotational direction around the arc axis [32, 38], which induces a horizontal rotating flow around the arc axis. This rotating motion generates a centrifugal force pushing plasma radially outward from the arc center, reducing the pressure at the central region of the arc column. Consequently, a strong pressure gradient develops between the upper and lower regions of the arc, accelerating plasma downward toward the weld pool surface. When this high-velocity plasma jet impacts the weld pool surface, the arc pressure significantly increases, creating a pronounced depression in the weld pool surface. This phenomenon allows the arc heat to penetrate deeper into the base metal, thus enhancing weld penetration, as observed in Fig. 6b.

These simulation results reasonably explain the intensified plasma flow velocity under EMF conditions to increase the metal vapor concentration around the axis, ultimately clarifying the deeper weld penetration obtained when EMF is applied.

Figure 12 presents the predicted influence of MFD on the maximum vertical velocity at the arc center obtained through numerical simulations for further discussion on the velocity of the plasma arc. It illustrates the relationship between the downward and upward plasma flow velocities within the arc column under varying magnetic flux densities. As indicated, the downward flow velocity at the center initially increases significantly with the magnetic flux density, reaching a peak near 700 m/s at approximately 35 mT. However, a further increase in magnetic flux density above

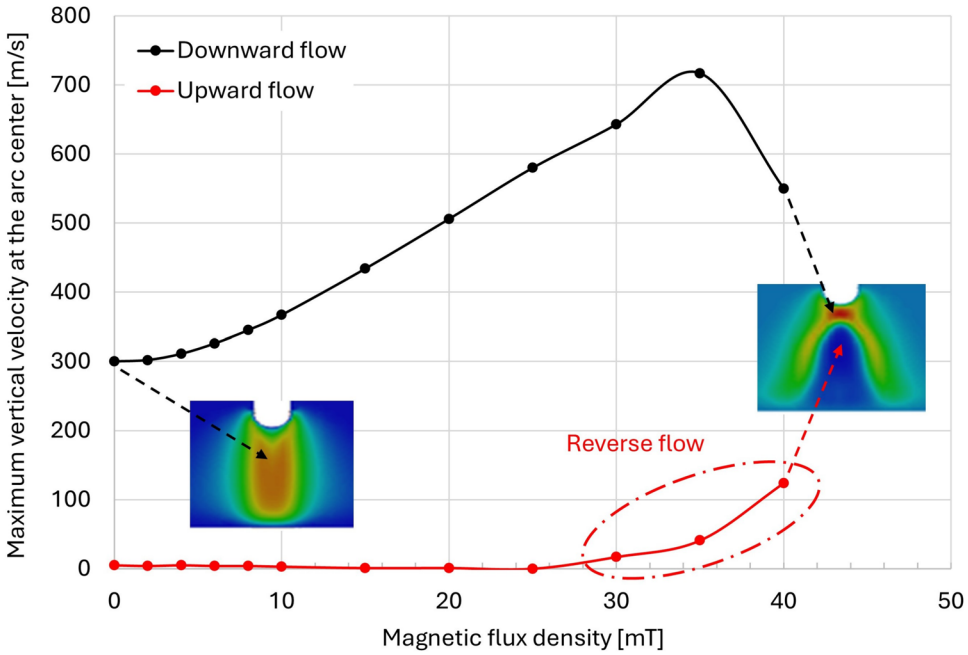

Fig. 12 Predicted influence of MFD on the maximum vertical velocity at the arc center

this threshold results in a marked decrease in downward flow velocity. Concurrently, a noticeable reverse or upward flow emerges, becoming apparent at magnetic flux densities exceeding approximately 30 mT. Considering strong EMF can destabilize metal transfer, this study primarily limited the applied magnetic flux density to a maximum of 6 mT. The numerical simulation was performed assuming the constant droplet temperature and ignoring the growth and also disturbance of it by EMF, so the results just present predictions under hypothetical conditions.

The velocity calculation indicates a transition in arc behavior under the application of longitudinal magnetic fields, analogous to phenomena observed in tungsten inert gas (TIG) welding arcs. Jian et al. reported similar behavior, where increasing the external magnetic flux density initially promoted the downward plasma flow velocity [39]. However, at higher flux densities (above 30 mT with a welding current of 300 A), a reverse plasma flow occurred, creating a negative pressure zone near the arc center due to strong electromagnetic stirring effects. This phenomenon, known as anti-gravity gradient or reverse flow behavior, reflects a significant alteration in the arc dynamics caused by the electromagnetic forces.

Nevertheless, the detailed dependence of downward plasma velocity on magnetic flux density in the current study differs notably from previous TIG welding studies. In TIG welding, the reduction in downward flow velocity and onset of reverse flow at high magnetic flux densities has been attributed mainly to electromagnetic stirring and negative pressure effects arising from a significant radial temperature gradient within the arc plasma [39, 40]. In contrast, the present study employs MCAW, where the presence and influence of metal vapor significantly alter arc plasma characteristics. The increased iron vapor concentration around the droplet region will modify the current path and, consequently, the electromagnetic force distribution within the arc. Furthermore, in the study of Jian et al., the current density was specified at the electrode tip as a function of position, so the arc root was fixed independent of the LMF condition [39]. This difference is expected to affect the results significantly. These phenomena require further investigation in future studies.

The results presented in this study further clarify the influence of EMF on the arc characteristics in MCAW processes. Compared to previous investigations applying LMF predominantly with conventional solid wires (GMAW processes) for reducing the spatter generation [32], the present study highlights distinct differences for metal-cored wires. For solid wires, the application of EMF at high welding currents typically induces significant rotational arc motion together with the molten metal column as a rotating transfer mode, dispersing heat energy radially outward and consequently reducing weld penetration, as reported by Yin et al. [41]. In contrast, this investigation demonstrates that for metal-cored wires, the mass of the droplet is large even at the high current, so the transfer mode does not become the rotating transfer but the globular or project transfer. Therefore, the arc does not exhibit substantial rotation under EMF conditions. Instead, the Lorentz force effectively constricts the arc and significantly intensifies the plasma velocity along the arc axis toward the weld pool, resulting in deeper weld penetration. These novel insights underline the potential

applicability of EMF in optimizing MCAW processes, especially in advanced manufacturing applications where precise control over weld geometry and penetration is critical, such as in additive manufacturing.

4 Conclusion

This study investigated the influence of an external longitudinal electromagnetic field (EMF) on arc behavior, weld pool dynamics, and weld penetration in the MCAW process between two conditions: without EMF and MFD of 6 mT. The conclusions can be summarized as follows:

- Application of a 6 mT EMF significantly increased arc brightness and concentrated the arc, leading to a deeper weld penetration compared with no EMF.
- Numerical simulations revealed that the applied EMF induced rotational plasma flow around the arc axis, resulting in reduced arc pressure at the arc center and increased plasma velocity toward the weld pool.
- The enhanced plasma velocity significantly increased arc pressure acting upon the weld pool surface, which produced a pronounced crater depression and notably increased weld penetration depth from 3.7 to 4.2 mm when MFD of EMF increased from 0 to 6 mT.

The submitted work was an original research study that has not been published previously and not under consideration for publication elsewhere, in whole or in part.

Acknowledgements The authors extend their gratitude to JWRI International Joint Research Collaboration (JIReC) 2024 program for facilitating this research and contributing to the collaborative relationship.

Author contribution Conceptualization: Shinichi Tashiro, Van Hanh Bui; methodology: Lei Xiao; formal analysis and investigation: Dang Khoi Le; writing—original draft preparation: Quang Ngoc Trinh; writing—review and editing: Shinichi Tashiro, Anthony B. Murphy; funding acquisition: Quang Ngoc Trinh, Shinichi Tashiro, Lei Xiao; resources: Le Duy Han, Huy Le Phan, Kenta Yamanaka; supervision: Manabu Tanaka.

Funding Open Access funding provided by The University of Osaka. This research is funded by Hanoi University of Science and Technology (HUST) under project number T2023-TĐ-020. This fund supported Quang Ngoc Trinh. This work is supported by JSPS KAKENHI (Grant Number JP21K04710), the Project on Design & Engineering by Joint Inverse Innovation for Materials Architecture (DEJI2MA) from the Ministry of Education, Culture, Sports, Science and Technology (MEXT), an OU Master Plan Implementation Project promoted under Osaka University. These funds supported Shinichi Tashiro. This research is funded by Natural Science Foundation of Gansu Province, China, Grant No. 21JR11RA057; Lanzhou Jiaotong University-Tianjin University Joint Innovation Fund Project, grant number LH2023001. These funds supported Lei Xiao.

Data Availability Data can be made available based on the requirements to verify this work.

Declarations

Consent to participate I would like to declare on behalf of my co-authors that all authors declare their full consent to participate in this research.

Consent for publication The authors confirm their agreement to the publication of this manuscript.

Competing interests The authors declare no competing interests.

References

1. Brien AO (1980) Welding Handbook. Macmillan Education UK, London
2. DebRoy T, David SA (1995) Physical processes in fusion welding. Rev Mod Phys 67:85–112. https://doi.org/10.1103/RevModPhys.67.85
3. Suzuki R (2012) State of the art of process control of molten droplet and pool in gas metal arc welding. Weld Int 26:178–186. https://doi.org/10.1080/09507116.2011.590663
4. Starling CMD, Modenesi PJ (2007) Metal transfer evaluation of tubular wires. Weld Int 21:412–420. https://doi.org/10.1080/09507110701510832
5. Bauné E, Bonnet C, Liu S (2001) Assessing metal transfer stability and spatter severity in flux cored arc welding. Sci Technol Weld Join 6:139–148. https://doi.org/10.1179/136217101101538677
6. Kim CJ, Seo BW, Son HJ et al (2024) Slag inclusion-free flux cored wire arc directed energy deposition process. Mater Des. https://doi.org/10.1016/j.matdes.2024.112669
7. Bui HV, Trinh NQ, Tashiro S et al (2023) Individual effects of alkali element and wire structure on metal transfer process in argon metal-cored arc welding. Materials. https://doi.org/10.3390/ma16083053
8. Kah P, Latifi H, Suoranta R et al (2014) Usability of arc types in industrial welding. International Journal of Mechanical and Materials Engineering 9(1):15
9. Zhai W, Wu N, Zhou W (2022) Effect of interpass temperature on wire arc additive manufacturing using high-strength metal-cored wire. Metals 12:020212. https://doi.org/10.3390/met12020212
10. Trinh NQ, Tashiro S, Tanaka K et al (2021) Effects of alkaline elements on the metal transfer behavior in metal cored arc welding. J Manuf Process 68:1448–1457. https://doi.org/10.1016/j.jmapro.2021.06.061
11. Valensi F, Pellerin N, Pellerin S et al (2018) Influence of wire initial composition on anode microstructure and on metal transfer

mode in GMAW: noteworthy role of alkali elements. Plasma Chem Plasma Process 38:177–205
12. Trinh NQ, Tashiro S, Suga T et al (2022) Metal transfer behavior of metal-cored arc welding in pure argon shielding gas. Metals 12:1577. https://doi.org/10.3390/met12101577
13. Trinh NQ, Tashiro S, Le KD et al (2024) Eligible CO2 content in Ar-CO2 mixture shielding gas for improving metal transfer in metal-cored arc welding. Int J Heat Mass Transfer. https://doi.org/10.1016/j.ijheatmasstransfer.2024.125803
14. Trinh NQ, Le KD, Tashiro S et al (2024) Optimization of metal transfer in rutile flux-cored arc welding through controlled CO2 concentration in argon–CO2 shielding gas. J Manuf Process 124:590–603. https://doi.org/10.1016/j.jmapro.2024.06.047
15. Pixner F, Buzolin R, Zelić A et al (2022) Tailoring the alloy composition for wire arc additive manufacturing utilizing metal-cored wires in the cold metal transfer process. Mater Des. https://doi.org/10.1016/j.matdes.2022.110453
16. Zavdoveev A, Klapatyuk A, Baudin T et al (2023) Non-equimolar cantor high entropy alloy fabrication using metal powder cored wire arc additive manufacturing. Additive Manufacturing Letters. https://doi.org/10.1016/j.addlet.2023.100124
17. Iqbal H, Pardal G, Suder W et al (2024) Experimental investigations on solid and metal-cored creep-resistant wires deposited under GMA and PTA-based wire arc additive manufacturing (WAAM). Int J Adv Manuf Technol. https://doi.org/10.1007/s00170-024-14926-5
18. Fan HG, Kovacevic R (1999) Droplet formation, detachment, and impingement on the molten pool in gas metal arc welding. Metall Mater Trans B 30:791–801. https://doi.org/10.1007/s11663-999-0041-6
19. Mvola B, Kah P (2017) Effects of shielding gas control: welded joint properties in GMAW process optimization. Int J Adv Manuf Technol 88:2369–2387
20. Zong R, Chen J, Wu C, Padhy GK (2016) Influence of shielding gas on undercutting formation in gas metal arc welding. J Mater Process Technol 234:169–176. https://doi.org/10.1016/j.jmatprotec.2016.03.020
21. Zeng M, Li ZT, Hu ZX et al (2023) The effects of welding parameters on metal transfer and bead properties in the variable-polarity GMAW of mild steel. Int J Adv Manuf Technol 129:4165–4183. https://doi.org/10.1007/s00170-023-12579-4
22. Alemdar ASA, Jalal SR, Mulapeer MMS (2022) Influence of friction stir welding process on the mechanical characteristics of the hybrid joints AA2198-T8 to AA2024-T3. Adv Mater Sci Eng 2022:1. https://doi.org/10.1155/2022/7055446
23. Alemdar ASA, Jalal SR, Mulapeer MM (2023) Effect of exfoliation corrosion on the efficient hybrid joint of AA2024-T3 and AA2198-T8 formed by friction stir welding. Heliyon. https://doi.org/10.1016/j.heliyon.2023.e16577
24. Huang Y, Zhang YM (2010) Laser-enhanced GMAW. Weld J 89:181S-188S
25. Fan Y, Yang C, Lin S et al (2012) Ultrasonic wave assisted GMAW. Weld J 91:91S-99S
26. Pal K, Pal SK (2011) Effect of pulse parameters on weld quality in pulsed gas metal arc welding: a review. J Mater Eng Perform 20:918–931. https://doi.org/10.1007/s11665-010-9717-y
27. Miao J, Li Y, Zhang S et al (2024) Magnetic controlled arc welding technology: a review. Rapid Prototyping J. https://doi.org/10.1108/RPJ-06-2023-0201
28. Luo J, Luo Q, Wang X, Wang X (2010) Ems-co2 welding: a new approach to improve droplet transfer characteristics and welding formation. Mater Manuf Process 25:1233–1241. https://doi.org/10.1080/10426914.2010.481000
29. Jiang SY, Wang XW, Chen HM, Liu P (2012) The impact of adscititious longitudinal magnetic field on CO 2 welding process. Adv Mater Res. https://doi.org/10.4028/www.scientific.net/AMR.538-541.1447
30. Wu C, Yang F, Gao J (2016) Effect of external magnetic field on weld pool flow conditions in high-speed gas metal arc welding. Proc Inst Mech Eng B J Eng Manuf 230:188–193. https://doi.org/10.1177/0954405414555591
31. Guan ZQ, Zhang HX, Liu XG et al (2019) Effect of magnetic field frequency on the shape of GMAW welding arc and weld microstructure properties. Mater Res Express. https://doi.org/10.1088/2053-1591/ab2572
32. Le DK, Tashiro S, Xu B et al (2025) Effects of longitudinal external magnetic field on metal transfer behavior and spatter formation in CO2 arc welding. Materials 18:030537. https://doi.org/10.3390/ma18030537
33. Tashiro S, Trinh QN, Le DK et al (2024) Elucidation of droplet detachment mechanism in metal-cored arc welding. J Manuf Process 124:1583–1605. https://doi.org/10.1016/j.jmapro.2024.07.040
34. Murphy AB (2010) The effects of metal vapour in arc welding. J Phys D Appl Phys 43:434001. https://doi.org/10.1088/0022-3727/43/43/434001
35. Murphy AB, Tam E (2014) Thermodynamic properties and transport coefficients of arc lamp plasmas: argon, krypton and xenon. J Phys D Appl Phys 47:295202. https://doi.org/10.1088/0022-3727/47/29/295202
36. Hertel M, Trautmann M, Jäckel S, Füssel U (2017) The role of metal vapour in gas metal arc welding and methods of combined experimental and numerical process analysis. Plasma Chem Plasma Process 37:531–547. https://doi.org/10.1007/s11090-017-9790-1
37. Schnick M, Füssel U, Hertel M et al (2010) Metal vapour causes a central minimum in arc temperature in gas-metal arc welding through increased radiative emission. J Phys D Appl Phys 43:022001. https://doi.org/10.1088/0022-3727/43/2/022001
38. Miao J, Li Y, Zhao H et al (2024) Study of CO2 welding arc with and without external magnetic field. J Braz Soc Mech Sci Eng. https://doi.org/10.1007/s40430-024-05265-3
39. Jian L, Zongxiang Y, Keliang X (2016) Anti-gravity gradient unique arc behavior in the longitudinal electric magnetic field hybrid tungsten inert gas arc welding. Int J Adv Manuf Technol 84:647–661. https://doi.org/10.1007/s00170-015-7728-4
40. Liu Y, Ding H, Luo J et al (2024) Numerical and experimental study of TIG welding arc in high frequency longitudinal magnetic field. J Mater Res Technol 33:5253–5262. https://doi.org/10.1016/j.jmrt.2024.10.181
41. Yin X, Gou J, Zhang J, Sun J (2012) Numerical study of arc plasmas and weld pools for GTAW with applied axial magnetic fields. J Phys D Appl Phys 45:285203. https://doi.org/10.1088/0022-3727/45/28/285203